KINEMATIC CHARACTERISTICS OF STEALTH CME IN THREE-DIMENSIONAL SPACE

Ya.I. Egorov (iD)
Institute of Solar-Terrestrial Physics SB RAS,
Irkutsk, Russia, egorov@iszf.irk.ru

V.G. Fainshtein (iD)
Institute of Solar-Terrestrial Physics SB RAS,
Irkutsk, Russia, vfain@iszf.irk.ru

Abstract. We have studied and compared kinematic characteristics of the motion of coronal mass ejections (CMEs) in three-dimensional (3D) space for three groups of CMEs for the period 2008–2014. These CME groups include: (i) stealth CMEs, (ii) CMEs that originate on the front side of the Sun (for an observer on Earth) and are associated with X-ray flares and filament eruption, (iii) all CMEs registered during the given period. Stealth CMEs are CMEs that emerge on the front side of the Sun and are unrelated to X-ray flares, as well as to filament eruption. We compare kinematic and some physical characteristics of these CMEs with those of a separate group of CMEs, classified as stealth in [D'Huys et al., 2014]. After comparing the characteristics of the three CME groups (i)–(iii), we concluded that

stealth CMEs have, on average, the lowest velocity, kinetic energy, mass and angular size, central position angle, and also the angle φ between the direction of CME motion in the ecliptic plane and the Sun–Earth line and the angle λ between the direction of CME motion in 3D space and the ecliptic plane. We also discuss distributions of CMEs of different types by kinematic characteristics.

Keywords: Sun, coronal mass ejection, solar flare, filament eruption, kinematic characteristics of CME motion.

INTRODUCTION

Many coronal mass ejections (CMEs) recorded in the coronagraph field of view are associated with various manifestations of solar activity in the lower corona (also known as low coronal signatures (LCS)): flares, filament eruption, etc. At the same time, there are CMEs, detected by coronagraphs, which are unrelated to LCS. Robbrecht et al. [2009] have shown that CMEs without LCS can occur on the front side of the Sun. Later, the front-sided CMEs without LCS were termed as stealth coronal mass ejections (hereinafter, stealth CME). Ma et al. [2010] have compared features of CMEs accompanied and unaccompanied by LCS and have found a noticeable difference between them.

Some researchers have suggested that the absence of LCS during occurrence of CMEs may be due to characteristics of the equipment that records solar radiation (see, e.g., [Howard, Harrison, 2013]). This means that the formation of stealth CMEs is most likely accompanied by some kind of activity in the lower corona (small, probably short-term flares, small filament eruptions, etc.), but it cannot be detected by spacecraft (SC) equipment.

D'Huys et al. [2014] have studied perhaps one of the largest samples of stealth CMEs — 40 events. These authors have proposed that stealth CMEs should be understood as coronal mass ejections that occur on the front side of the Sun but are not accompanied by LCS. D'Huys et al. [2014] have examined features of selected stealth CMEs in quite sufficient detail. For example, the position angle of these CMEs often appeared to be close to 0° (or 360°, what is the same), although, in fact, it could take any value.

One of the most difficult problems in studying stealth CMEs is to prove that the CME observed has originated on the front side of the Sun. D'Huys et al. [2014] have proposed an original method for determining the side of the Sun (front or back for an observer on Earth) on which the CME observed simultaneously in the SOHO/LASCO and STEREO-A, -B COR2A and COR2B coronagraph fields of view was formed.

Alzate, Morgan [2017], using advanced methods of solar image processing in various spectral channels of AIA/SDO instruments, have found that the formation of each stealth CME from [D'Huys et al., 2014] is accompanied by some small-scale solar events. They concluded that all 40 stealth CMEs from [D'Huys et al., 2014] were associated with certain forms of LCS (jets or eruptions of small filaments, etc.). Alzate, Morgan [2017] concluded that the assignment of the CMEs listed in [D'Huys et al., 2014] to stealth CME group was due to the limitations of the spatial and temporal resolution of SDO/AIA telescopes and the use of unsatisfactory data preprocessing methods. Nevertheless, strictly speaking, the information about the activity, detected by Alzate, Morgan [2017], which accompany the occurrence of the CMEs from [D'Huys et al., 2014], is not enough to precisely localize the occurrence of these CMEs. This can be done most accurately by detecting the occurrence of the CME frontal structure, as, for example, in [Zagainova et al., 2020].

It is now believed that most (up to 80 %) filament eruptions are connected with CMEs [Schmieder et al., 2013]. Schmieder et al. [2013] have shown that in some cases a filament eruption triggers the formation of a

CME; and a mechanism of CME generation by eruptive filament has been proposed in [Fainshtein, Egorov, 2015]. Yet, as noted above, filament eruption does not precede stealth CME. On this evidence, we can assume that the generation mechanism of stealth CMEs differs from the generation mechanisms of many ordinary CMEs, but details of this mechanism remain unknown.

In this work, for the period 2008–2014 we have identified a group of CMEs emerging on the front side of the Sun (for an observer on Earth) and unrelated to X-ray flares of importance higher than B1.0, as well as to filament eruption. We classified them as stealth CMEs. In fact, we have proposed a method for automatic identification of stealth CMEs. For these CMEs, as well as for all CMEs analyzed and CMEs emerging on the front side of the Sun but related to X-ray flares and/or to filament eruptions, we have compared the CME kinematic characteristics measured in three-dimensional (3D) space. For these CME groups we have also compared the relative frequencies of occurrence of different kinematic characteristics of CME motion in 3D space. For these three CME groups and for the CMEs studied by D'Huys et al. [2014] and also those the authors classified as stealth CMEs, we have compared distributions of relative occurrence frequencies depending on their kinematic and other characteristics derived from LASCO data.

DATA AND ANALYSIS METHODS

Stealth CMEs are characterized by the absence of LCS; therefore, to select them from a huge number of events it is necessary to exclude the CMEs linked to filament eruption and flares, and also to study only those CMEs that occurred on the front side of the Sun since on the back side we cannot reliably establish the connection between CMEs and LSC. To determine the side of the Sun on which a CME emerges, we should find the φ angle between the direction of CME motion in the ecliptic plane and the Sun–Earth line (Figure 1). The φ angle (see Figure 1) takes positive values counterclockwise and negative ones clockwise from the Sun–Earth line. At $|\varphi|>90°$, a CME emerged on the back side of the Sun; at $|\varphi|\leq90°$, on the front side.

To find the φ angle of each CME considered, we employ the triangulation method described in [Egorov, Fainshtein, 2021], which involves using data from any pairs of SOHO coronagraphs (LASCO [Brueckner et al., 1995]) and STEREO-A and STEREO-B coronagraphs (Solar Terrestrial Relations Observatory [Kaiser et al., 2008]; COR2 coronagraphs; COR2 is part of SECCHI on board the STEREO spacecraft [Howard et al., 2008]). To calculate the φ angle, we use information about the CME position in the plane of the sky of the coronagraph. The data can be obtained from the CME catalogs for LASCO [https://cdaw.gsfc.nasa.gov/CME_list] and STEREO [http://spaceweather.gmu.edu/seeds/secchi], which also contain information about the position angle, angular size, projection linear velocity, and other CME parameters.

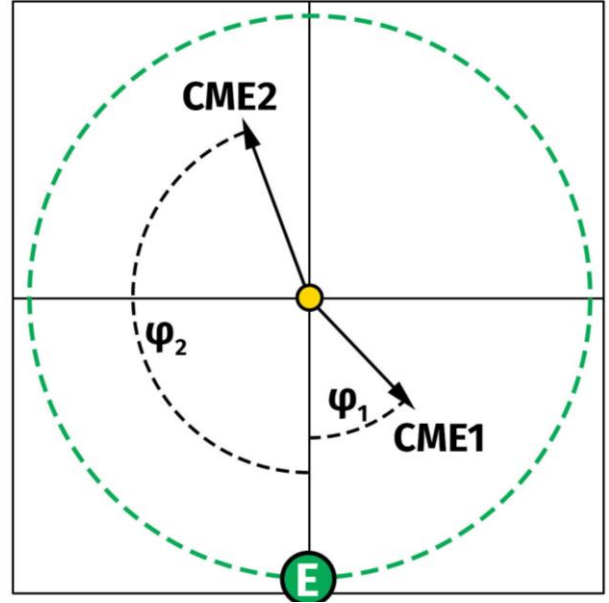The φ angle is determined using the relations we have derived [Egorov, Fainshtein, 2021]

Figure 1. Angle $\varphi<0$ clockwise and $\varphi>0$ counterclockwise from the Sun–Earth line. In the ecliptic plane are the Sun (yellow circle), Earth (green circle), and motion directions of two CMEs (black arrows). CME1 emerged on the front side of the Sun; CME2, on the back side of the Sun

$$\varphi_{1,\,2} = \operatorname{atan}\left(\frac{S\sin b - \sin a}{S\cos b + \cos a}\right) \pm n\pi,\, n \in [0,1],$$

$$\varphi_{3,\,4} = \operatorname{atan}\left(\frac{S\sin b + \sin a}{\cos a - S\cos b}\right) \pm n\pi,\, n \in [0,1].$$

Here $S=S_A/S_B$, where S_A, S_B are radial distances from the center of the Sun to the boundary of CME projection in the plane of the sky of two coronagraphs on the ecliptic plane (be specific, assume that these are COR2A and COR2B coronagraphs); a and b are the angles between the Sun—Earth and Sun – STEREO-A/STEREO-B SC lines respectively. System of equations (1)–(2) has four solutions. To choose the only correct solution, the CME motion direction relative to the central meridian (to the east or to the west) in the LASCO C2 field of view, as well as in the field of view of each coronagraph, is taken into account.

We also use the distances R_{3D} of the CME boundary relative to the center of the Sun in 3D space:

$$R_{3D} = \left[\frac{S_A}{|\sin(\varphi - a)|}\right]\Big/\cos\lambda.$$

Here, λ is the angle between the CME motion direction in 3D space and the ecliptic plane, which in this case we consider coincident with the plane of the solar equator:

$$\lambda = \operatorname{atan}(\operatorname{tg}\Lambda\sin|\varphi|),$$

where Λ is the angle between the CME motion direction and the ecliptic plane in the LASCO C2 plane of the sky: $\Lambda>0$ if CME moves to the north of the plane of the solar equator, and $\Lambda<0$ if CME moves to the south of the equator plane. The λ angle has similar signs. Formula (3) allows us to find the CME velocity in 3D space:

$$V_{3D} = dR_{3D}(t)/dt.$$

In this work, we explore properties of CMEs of different types for the period from 2008 through 2014, when all three coronagraphs were in operation. During the period, 6850 events were recorded in the LASCO catalog, with estimated CME mass and energy. The CMEs for which there is no data available are not suited for the study because they are poorly visible in the coronagraph field of view or their measurements are available for a small number of time points. The STEREO-A and -B catalogs contain respectively 7809 and 9529 events suitable for the analysis.

We have analyzed three CME groups. The first group is stealth CMEs, i.e. the CMEs that emerge on the front side of the Sun and are unrelated to X-ray flares of importance >B1.0 and to eruptive filaments recorded within two hours relative to the moment of the first appearance of CME in the LASCO C2 field of view. The second group includes CMEs that emerge on the front side of the Sun and are connected with X-ray flares and/or filament eruption. We have designated this CME group as FSCME with LCS. Here FSCME is Front Side Coronal Mass Ejection, i.e. the CMEs that originate on the front side of the Sun. The third group is designated All CMEs. This group includes stealth CME, FSCME with LCS, and all CMEs detected on the back side of the Sun.

Most of the plots in this paper show the relative frequency of occurrence (*RF*) of a parameter as a function of another parameter. By definition, *RF* is the percentage of CMEs of a certain type to all CMEs of this type considered, which varies depending on a CME feature (e.g., on the year of observation of the CME, see Figure 3).

Let us describe the procedure for sequentially excluding events from the general sample, which allows us to identify stealth CMEs:

1. Distribution of events from different catalogs by pairs of coronagraphs, necessary for the application of the method of determining the side of the Sun on which CME emerged [Egorov, Fainshtein, 2021]. To be certain that the events from different catalogs refer to the same CME, we have introduced the following criteria: the time of the first measurement of the CME position in the catalogs should not differ by more than an hour and

a half; the event should be recorded by both devices in the same hemisphere — southern or northern (Figure 2, *a*). To these criteria correspond 2876 CMEs simultaneously observed by LASCO C2 and COR2A coronagraphs; 2004 CMEs, by COR2A and COR2B; 2806 CMEs, by LASCO C2 and COR2B. At the same time, during the period under study (2008–2014) LASCO C2 recorded 6850 CMEs; COR2A, 7809 CMEs; COR2B, 9529 CMEs (Figure 2, *a*).

2. Selecting events for which simultaneous measurements by more than one pair of spacecraft are available.

3. Calculating and comparing φ angles for each event derived from data from different pairs of coronagraphs, and excluding events for which the difference in the angles obtained exceeds 10° in modulus.

4. Excluding the back-sided events, which corresponds to φ|>90°.

5. Excluding the flare associated CMEs that are in the catalog [https://www.ngdc.noaa.gov/stp/space-weather/solar-data/solar-features/solar-flares/x-rays/goes/xrs].

6. Excluding the CMEs associated with filament eruption, which are in the catalog [https://cdaw.gsfc.nasa.gov/CME_list/autope].

Thus, we have identified 96 stealth CMEs for the period 2008–2014. The stealth CMEs are listed in Appendix.

The number of events remaining after each step from the above list of necessary steps is shown in Figure 2, *b*. All procedures discussed in paragraphs 1–6 are automated; special programs have been developed for their implementation.

RESULTS

Below we compare characteristics of three CME groups: 1) stealth CMEs, 2) FSCME with LCS, and 3) all CMEs recorded during the said period. In addition, in some cases we consider CMEs assigned to stealth CMEs [D'Huys et al., 2014].

Figure 3 illustrates time variation in the relative frequency (*RF*) of occurrence of CMEs of each group considered during the year. It is apparent that the percentage
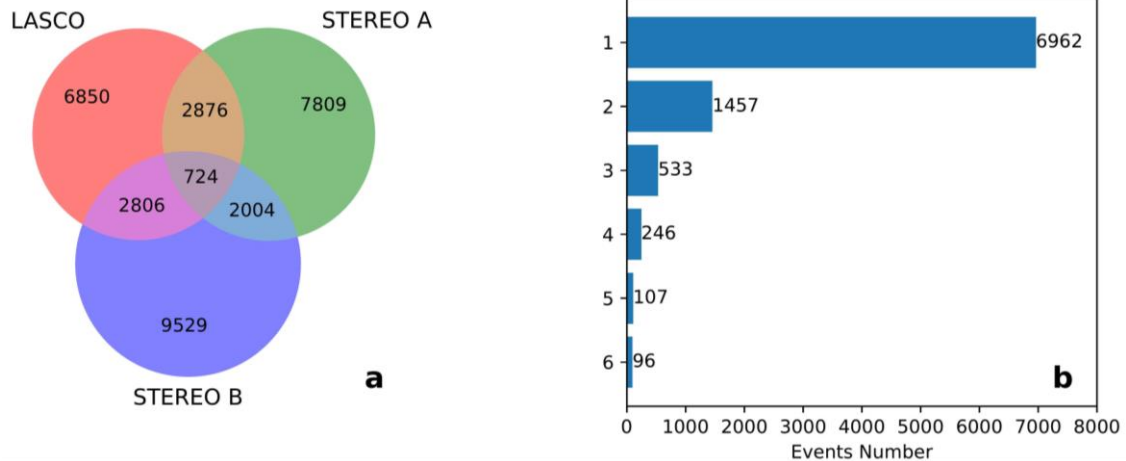

Figure 2. Samples from different CME catalogs recorded by different coronagraphs, with indication of the number of events (*a*); the number of events in pairs of samples at each stage of the procedure described in Section "Data and Analysis Methods" in paragraphs 1–6 (*b*)
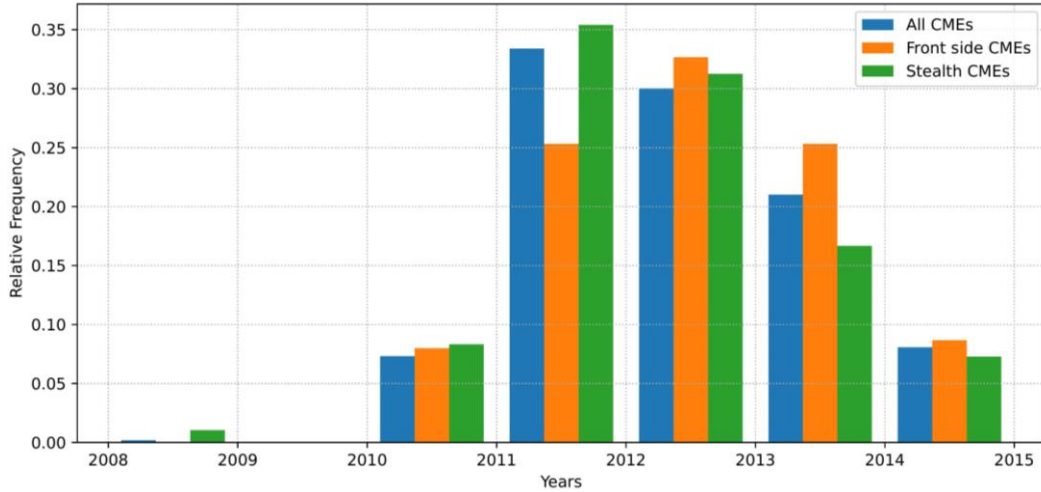
Figure 3. Time variation in the relative frequency of occurrence of stealth CMEs, FSCME with LCS, and all CMEs recorded over the period 2008–2014.

of stealth CMEs exceeds that of CMEs of other types in 2010, near the solar minimum, and during its increase in 2011; and it is lower than the percentage of other CME groups in 2013–2014 — during the solar maximum. In 2012, the percentage of stealth CMEs is higher than that of all CMEs and lower than the percentage of FSCME with LCS. Our analysis has revealed that the time variation in the relative frequency of occurrence of CMEs of each group considered differs. For stealth CMEs, *RF* drops sharply to the left of the maximum in 2011 and changes relatively slowly to the right of the maximum value. *RF* for FSCME with LCS has a wide peak depending on time with maximum in 2012 and features the lowest and highest values among the three groups of interest in 2011 and 2012–2014 respectively. The *RF* distribution as a function of time for the All CME group has a rather asymmetric shape relative to the maximum value, similar to the shape of the distribution for stealth CMEs. We do not discuss the *RF* values in 2008 due to the large error in determining CME parameters during

this period, associated with small deviations of the STEREO-A, -B spacecraft from Earth.

Figure 4 for the three CME groups compares *RF* distributions depending on longitude (angle φ) and latitude (angle λ) in 3D space. It follows from Figure 4 that CMEs from the stealth-CME and FSCME with LCS groups are concentrated near the angles φ=–50° and φ=50°, with the number of stealth CMEs being larger in the vicinity of φ=–50°. CMEs from the All CME group with close relative frequency values were at φ=–170°, –50°, and 30°; and with a slightly increased relative frequency, at φ=110°. The *RF*(λ) distributions for the stealth-CME and All CME groups have a bell shape (i.e. *RF* decreases in both directions as it moves away from λ, at which *RF* is maximum). The *RF* decrease rate for stealth CMEs in the left part of the *RF*(λ) distribution turned out to be higher than for all CMEs. The *RF*(λ) distribution for FSCME with LCS reached a plateau after the initial decrease to the left of the maximum.
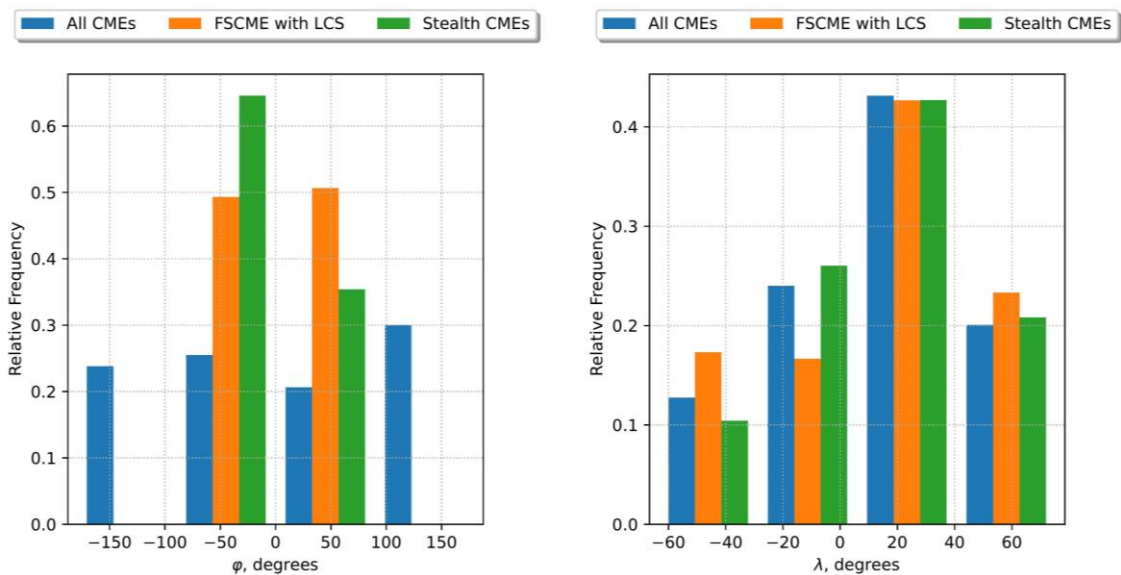

Figure 4. Relative frequency of occurrence of CMEs of the stealth-CME, FSCME with LCS and All CME groups as a function of longitude (angle φ) and latitude (angle λ) in 3D space

Figure 5 shows the relationship of the φ and λ angles with the CME central position angle *CPA* (the position angle of the CME axis passing from the center of the Sun through the middle of the CME) in the plane of the sky of LASCO coronagraphs for the stealth-CME, FSCME with LCS, and All CME groups. For all the groups, the number of CMEs is approximately equally distributed relative to φ=+/–90°, as well as on the front (φ=0–90° and φ=0÷–90°) or back (φ=90°–180° and φ=–90°–180°) side of the Sun. The relationship of λ with *CPA* for all the CME groups considered, as expected, appeared to be linear with opposite slope angle in the *CPA* range 0–180° and 180°–360°.

We have investigated and compared the relationship of the velocity of motion in 3D space V_{3D} with the φ and λ angles for the three CME groups (Figure 6). For φ angles (see Figure 6, top panels), we present the distribution of the number of events in rectangles 200 km/s×40° for the All CME group and 200 km/s×20° for the FSCME with LCS and stealth-CME groups. Figure 6 suggests that the maximum number of events for all CMEs (top left panel) is recorded in rectangles centered at (300 km/s, –130°), (300 km/s, 0°); for FSCME with LCS (top middle panel), in a rectangle centered at (300 km/s, 20°); and for stealth CMEs (top right panel), in a rectangle centered at (300 km/s, 0°).

Three bottom panels of Figure 6 illustrate CME velocity distributions — the λ angle for the three CME groups in rectangles 200 km/s×20°. We can see that the maximum number of events for the All CME group (left) is in a rectangle centered at (500 km/s, 40°); for FSCME with LCS (middle), in a rectangle centered at (700 km/s, 40°); and for stealth CMEs (right), in a rectangle centered at (300 km/s, 40°).

Figure 7 depicts the distribution of the number of events as a function of CME velocity in 3D space for the three CME groups in different years of the observation period. The dependence of the number of events is shown in rectangles 100 km/s×1 year. Figure 7 indicates that the maximum number of events for the All CME group is recorded in a rectangle centered at (350 km/s, 2011); for FSCME with LCS, in a rectangle centered at (350 km/s, 2012); for stealth CMEs, in a rectangle centered at (350 km/s, 2011).

The results of calculations of kinematic characteristics of several CMEs in [Egorov, Fainshtein, 2021] have shown that as CME moves in 3D space the angle φ varies with time. We tried to figure out to what extent the rate of change of φ with distance is related to the parameters of CME motion: *CPA*, λ, and CME velocity. The corresponding dependencies for the three CME groups are displayed in Figure 7. For each CME considered we have plotted φ versus the distance from the center of the Sun in 3D space R_{3D}, approximated by linear regression. We utilized the slope of this line to the horizontal axis R_{3D} as a characteristic of the rate of φ change with height — $d\varphi/dR_{3D}$.

Referring to Figure 8, for most CMEs in the three CME groups $-2°/R_s < d\varphi/dR_{3D} < 2°/R_s$ (R_s is the solar radius) for the entire range of variation in the parameter analyzed. For each CME group there is a range of variation in the parameters considered, within which $-5°/R_s < d\varphi/dR_{3D} < 5°/R_s$: for *CPA*, this is a neighborhood of the angles of ~50° and 320°; for λ, a neighborhood of the angle of 25°; for the CME velocity, ~400 km/s.

Note that for each parameter in each group there are CMEs for which $-10°/R_s < d\varphi/dR_{3D} < -5°/R_s$ and $5°/s < d\varphi/dR_{3D} < 10°/R_s$. The coronal mass ejections from the All CME group largely fall into these ranges of the rate of φ change with height. We have not managed to explain this effect yet. It is also difficult to explain that according to visual observations FSCME with LCS more often go beyond the range $-5°/R_s < d\varphi/dR_{3D} < 5°/R_s$ than stealth CMEs.

Figure 9 presents relative frequencies *RF*, determined from LASCO data, of different values of CME linear projection velocity, acceleration, kinetic energy, angular size, and mass for our stealth-CME and FSCME with [D'Huys et al., 2014]. The CME characteristics were taken from the SOHO LASCO CME Catalog [https://cdaw.gsfc.nasa.gov/CME_list]. Note that of the 40 stealth CMEs discussed in [D'Huys et al., 2014], we have found only 20 events in this catalog. Figure 9 indicates that the nature of the change in the relative frequency of occurrence of CMEs of one type differs in the selected parameter (CME characteristic) for different CME parameters, but is approximately the same for a given
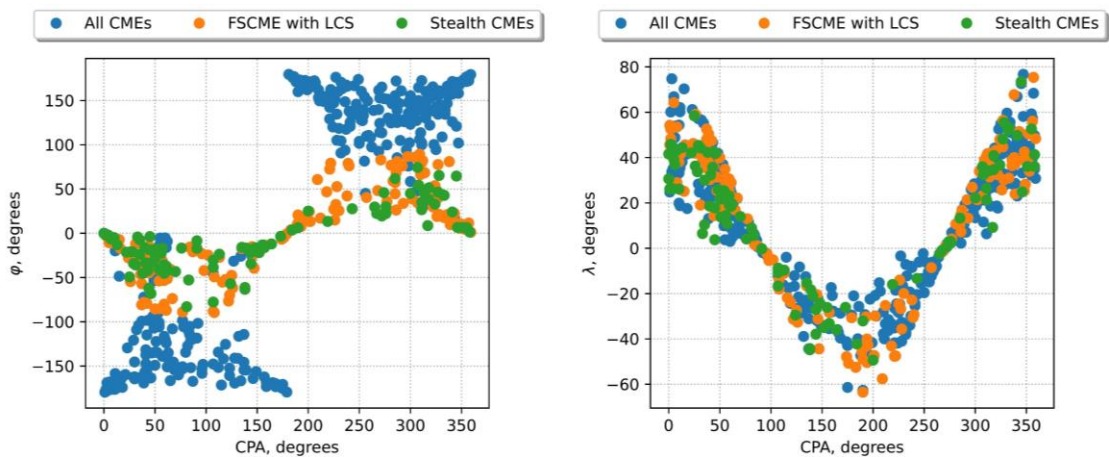

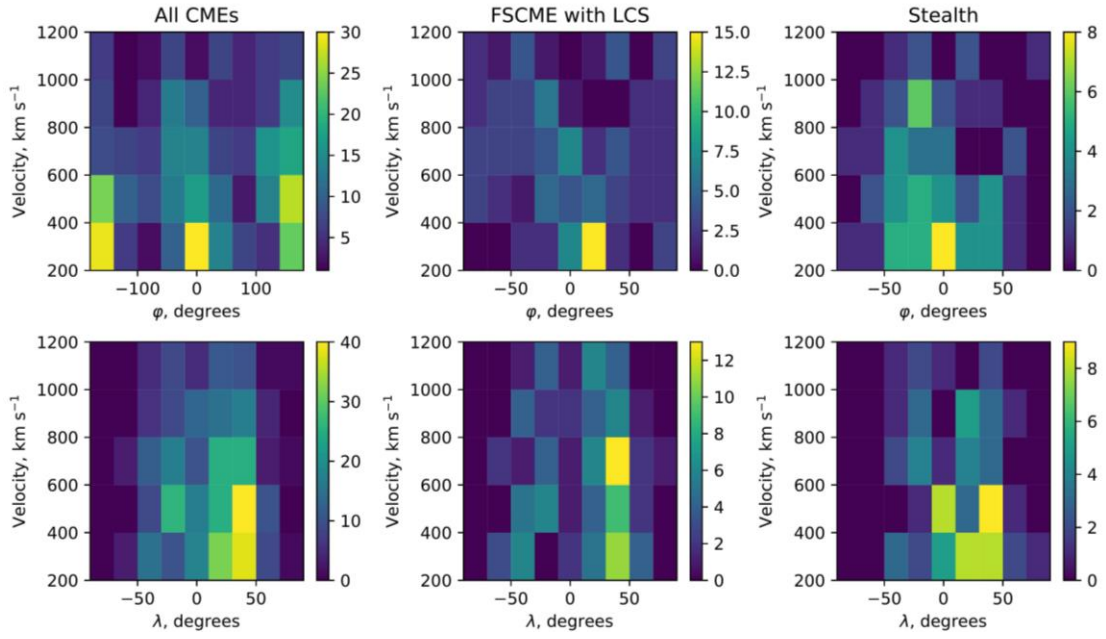*Figure 5*. Angles φ and λ as a function of *CPA* in the plane of the sky of LASCO coronagraphs for the three CME groups

Figure 6. Maps of the number of CMEs in rectangles of a given size as a function of CME velocity in 3D space and the φ and λ angles (top and bottom panels respectively). The number of CMEs is shown by the color scale to the right of the panel
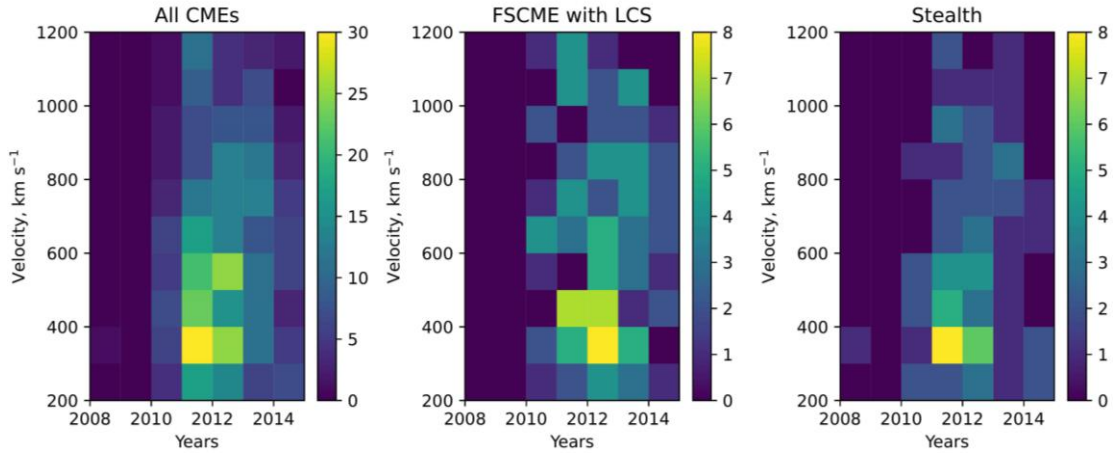

Figure 7. Maps of the number of CMEs in rectangles of a given size as a function of CME velocity in 3D space and the year of CME observation. The number of CMEs is shown by the color scale to the right of the panel
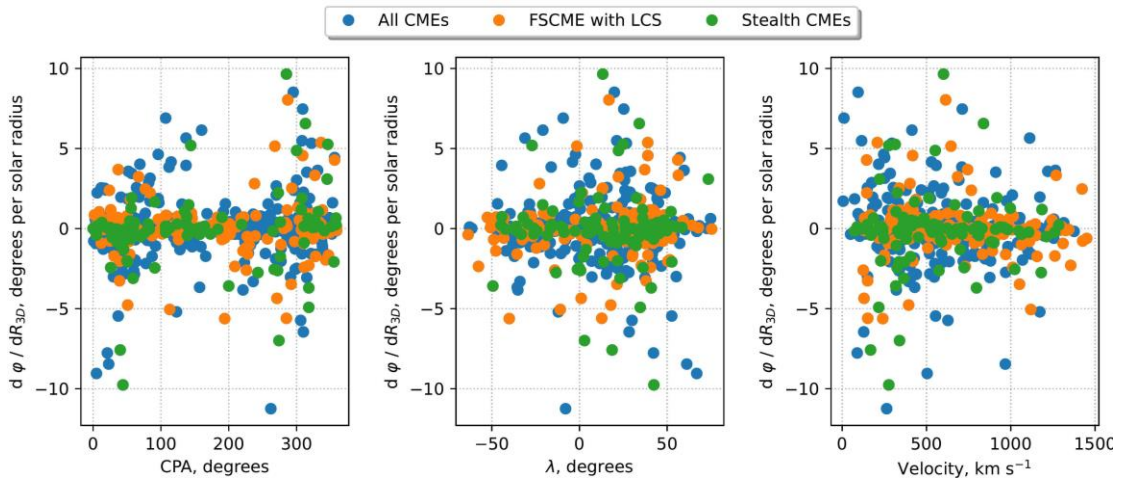

Figure 8. Rate of φ change as a function of *CPA*, λ, and velocity in 3D space for the three CME groups
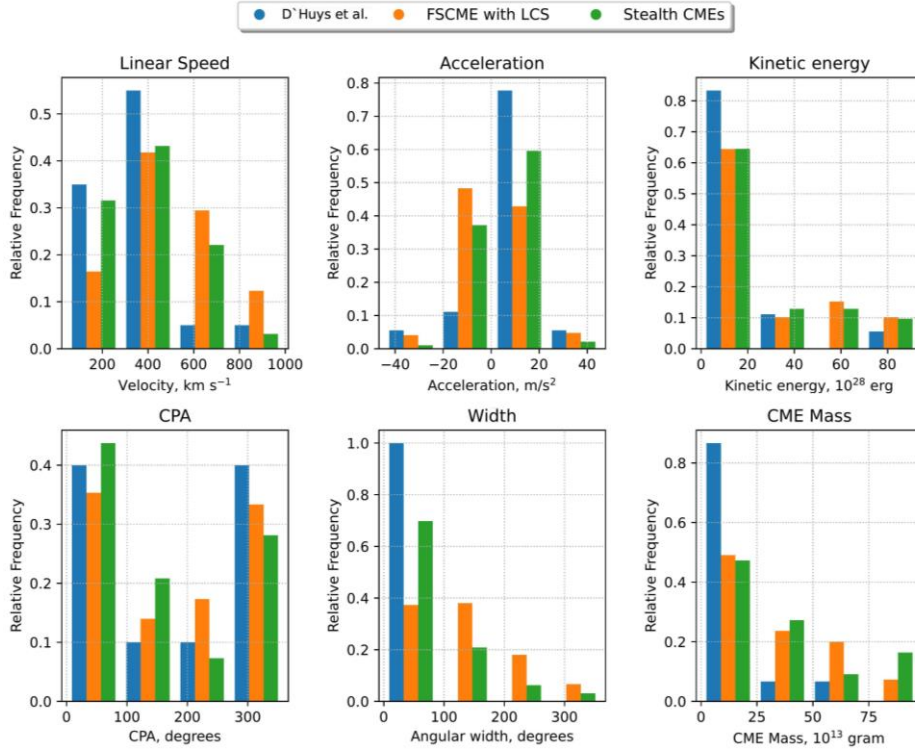
Figure 9. Relative frequency of occurrence of CMEs with different parameters for three CME groups: stealth CMEs from [D'Huys et al., 2014], FSCME with LCS and stealth CMEs we have selected

parameter of CMEs of different types. For example, the dependence of the relative frequency of occurrence of CME on the linear projection velocity turns out to be bell-shaped; whereas on the central position angle (*CPA*),LCS groups, as well as for the stealth-CME group from close to parabolic. It also follows from Figure 9 that the velocity, kinetic energy, mass, angular size of the stealth CMEs from [D'Huys et al., 2014] are on average less than similar parameters of our stealth CMEs (see also Table). From a plot of *RF* versus *CPA* it follows that minimum *CPA* values for the three CME groups are in the vicinity of 215°, and maximum *RF* values are near *CPA*=30° and 320°. For the kinetic energy, angular size, and mass, *RF* decreases with increasing CME parameter.

Table lists the CME characteristics averaged over the above groups of events: A is the CME linear projection velocity (in km/s); B is the CME acceleration (in m/s^2); C is the energy (in 10^{29} erg); D is the CME central position angle (in degrees); E is the CME angular size (in degrees); F is the CME mass (in 10^{13} g); G is the φ angle (in degrees), H is the λ angle (in degrees). The number of events in a group is given in parentheses.

CONCLUSION

Until recently, individual stealth CMEs or small groups of such CMEs have mainly been studied. We have proposed a method of automatic identification of stealth CMEs during an arbitrary period when CMEs could be observed by more than one pair of spaced coronagraphs. Thus, over a long period of time we can identify a large number of stealth CMEs and investigate their properties. In this case, we define stealth CMEs as coronal mass ejections that occur on the front side of the Sun and are not associated with X-ray flares and eruptive filaments, as derived from catalogs of these processes. The side of the Sun on which stealth CMEs emerged was determined using the method of finding the direction of CME motion in 3D space [Egorov, Fainshtein, 2021]. We have thus identified 96 stealth CMEs over the period 2008–2014.

In this paper, we have compared properties of three CME groups: 1) stealth CMEs (96 events); 2) FSCME with LCS, 150 events; 3) all CMEs considered under the approach described in Section "Data and Analysis Methods" (533 events).

	A	B	C	D	E	F	G	H
Stealth CMEs (96)	399±40	10±3	26±16	149±24	84±13	16±6	28±4	27±3
Front-sided CMEs (150)	530±47	10±2	130±98	174±19	129±13	36±10	37±4	33±2
Back-sided CMEs (287)	414±24	10±1	39±18	187±13	97±9	17±3	146±2	27±1
All CMEs (533)	444±20	10±1	62±29	177±10	103±6	22±3	94±5	29±1
D'Huys et al. (20)	351±74	29±9	2±1	178±68	44±12	7±5		

Our analysis has shown that the relative frequency *RF* of recording of stealth CMEs exceeds *RF* of occurrence of FSCME with LCS and all CMEs in 2011 and 2012, i.e. during solar activity minimum and increase. The nature of time variation in *RF* of occurrence of FSCME with LCS differs significantly from the similar *RF*(*t*) dependence for stealth CMEs: in the former case, the distribution of *RF*(*t*) relative to the maximum is quite symmetric, whereas in the latter it is strongly asymmetric with a sharper decrease to the left of the maximum.

For stealth CMEs, the average φ angle is shown to be 28° in modulus with a more frequent occurrence of this angle to the east of the Sun–Earth line in the plane of the solar equator (negative φ values). For FSCME with LCS this angle is 37°. The *RF*(λ) distribution has a clearly defined bell shape for stealth CMEs and a shape slightly different from the bell shape for FSCME with LCS. The positions of peaks of the *RF*(λ) distributions for the three CME groups coincide.

We have established a relationship of the φ and λ angles with the central position angle *CPA* in the plane of the sky of LASCO coronagraphs for all CME groups considered. Approximately the same number of stealth CMEs turned out to be in the *CPA* ranges 0°–180° and 180°–360°. The relationship between λ(*CPA*) and opposite slope angles in the *CPA* range 0°–180° and 180°–360° proved to be linear.

For the All CME, FSCME with LCS, and stealth-CME groups we have compare the CME velocity in 3D space V_{3D} with the φ and λ angles. We have found places of maximum localization of the number of CMEs in the planes V_{3D}–φ and V_{3D}–λ. So, for example, most stealth CMEs have been recorded in rectangles with the center coordinates (V_{3D}=300 km/s; φ=0°); (V_{3D}=500 km/s; λ=40°). We have determined distributions of the number of events depending on the CME velocity in 3D space for the three CME groups in different years of the observation period. The places of maximum localization of CMEs in the planes V_{3D}–years have been identified. Most stealth CMEs have been recorded in a rectangle with coordinates (V_{3D}=300 km/s; 2011).

In [Egorov, Fainshtein, 2021], we have shown that as CME moves in three-dimensional space the φ angle varies with time. In this paper, we have figured out to what extent the rate of φ change with distance is related to *CPA*, λ, and CME velocity in 3D space. For most CMEs in the three groups of events – $2°/R_s<d\varphi/dR_{3D}<2°/R_s$ for the entire range of variation of the parameter analyzed. At the same time, for each CME group there is a range of parameter variation, within which $-10°/R_s<d\varphi/dR_{3D}<10°/R_s$.

It is interesting to compare the properties of stealth CMEs and FSCME with LCS. CMEs of both groups emerged on the front side of the Sun, but stealth CMEs are not associated with solar flares and/or filament eruption, whereas FSCME with LCS are related to them. Averages of linear projection velocity, kinetic energy, central position angle, angular size, and mass of stealth CMEs are less than those of FSCME with LCS, and only accelerations are on average the same for these CME groups.

For stealth CMEs, FSCME with LCS, as well as for the stealth CMEs from [D'Huys et al., 2014], we have

calculated relative frequencies of occurrence for linear projection velocity, acceleration, kinetic energy, angular dimensions, and central position angle from LASCO data. We have established that the nature of the variation in the relative frequency of occurrence of CMEs of each type, depending on the selected parameter (CME characteristic), differs for different CME parameters, but is roughly the same for a given parameter for CMEs of different types. The velocity, kinetic energy, angular size, and mass of the stealth CMEs from [D'Huys et al., 2014] are shown to be less than the similar parameters of the stealth CMEs we have identified.

Appendix contains information about the stealth CMEs we have found. It is worth noting that the events have been selected automatically, using information on flares and eruptive filaments from the catalogs described in Section "Data and Analysis Methods". The planned in-depth study into the events from the list of stealth CMEs with the aid of multiwave EUV observations will probably provide a more detailed insight into the relationship between the selected CMEs and solar events in the lower corona. We believe that in the future the relationship between these CMEs and the small-scale and rapidly changing activity in the lower corona on the front side of the Sun will be investigated. The results of similar studies into two stealth CMEs identified by other researchers have been reported in [Zagainova et al., 2020].

REFERENCES

Alzate N., Morgan H. Identification of low coronal sources of stealth coronal mass ejections using new image processing techniques. *Astrophys. J.* 2017, vol. 840, article id. 103, 14 p. DOI: 10.3847/1538-4357/aa6caa.

Brueckner G.E., Howard R.A., Koomen M.J., Korendyke C.M., Michels D.J., Moses J.D., Socker D.G., et al. The Large Angle Spectroscopic Coronagraph (LASCO). *Solar Phys.* 1995, vol. 162, p. 357. DOI: 10.1007/BF00733434.

D'Huys E., Seation D., Poedts S., Berghmans D. Visualizing fuzzy overlapping communities in networks. *Astrophys. J.* 2014, vol. 795, iss. 1, article id. 49, 12 p. DOI: 10.1088/0004-637X/795/1/49.

Egorov Ya.I., Fainshtein V.G. A simple technique for identifying the propagation direction of CME in a 3D space. *Solar Phys.* 2021, vol. 296, iss. 9, article id. 126, 14 p. DOI: 10.1007/s11207-021-01904-3.

Fainshtein V.G., Egorov Ya.I. Initiation of CMEs associated with filament eruption, and the nature of CME related shocks. *Adv. Space Res.* 2015, vol. 55, iss. 3, pp. 798–807. DOI: 10.1016/j.asr.2014.05.019.

Howard T., Harrison R. Stealth coronal mass ejections: A perspective. *Solar Phys.* 2013, vol. 285, pp. 269–280. DOI: 10.1007/s11207-012-0217-0.

Howard R.A., Moses J.D., Vourlidas A., Newmark J.S., Socker D.G., Plunkett S.P., Korendyke C.M., et al. Sun Earth Connection Coronal and Heliospheric Investigation (SECCHI). *Space Sci. Rev.* 2008, vol. 136, iss. 1-4, pp. 67–115. DOI: 10.1007/s11214-008-9341-4.

Kaiser M.L., Kucera T.A., Davila J.M., St. Cyr O.C., Guhathakurta M., Christian E. The STEREO Mission: An

Introduction. *Space Sci. Rev.* 2008, vol. 136, iss. 1-4, pp. 5–16. DOI: 10.1007/s11214-007-9277-0.

Ma S., Attrill G.D.R., Golub L., Lin J. Statistical study of coronal mass ejections with and without distinct low coronal signatures. *Astrophys. J.* 2010, vol. 722, pp. 289–301. DOI: 10.1088/0004-637X/722/1/289.

Robbrecht E., Patsourakos S., Vourlidas A. No trace left behind: Stereo observation of a coronal mass ejection without low coronal signatures. *Astrophys. J.* 2009, vol. 701, pp. 283–291. DOI: 10.1088/0004-637X/701/1/283.

Schmieder B., Démoulin P., Aulanier G. Solar filament eruptions and their physical role in triggering coronal mass ejections. *Adv. Space Res.* 2013, vol. 51, iss. 11, pp. 1967–1980. DOI: 10.1016/j.asr.2012.12.026.

Zagainova Iu.S., Fainshtein V.G., Gromova L.I., Gromov S.V. Source region identification and geophysical effects of stealth coronal mass ejections. *J. Atmos. Solar-Terr. Phys.* 2020, vol. 208, article id. 105391. DOI: 10.1016/j.jastp.2020.105391.

URL: https://cdaw.gsfc.nasa.gov/CME_list (accessed March 30, 2022).

URL: http://spaceweather.gmu.edu/seeds/secchi (accessed March 30, 2022).

URL: https://www.ngdc.noaa.gov/stp/space-weather/solar-data/solar-features/solar-flares/x-rays/goes/xrs (accessed March 30, 2022).

URL: https://cdaw.gsfc.nasa.gov/CME_list/autope (accessed March 30, 2022).

APPENDIX

Stealth CMEs

A	B	C	D	E	F	G	H	A	B	C	D	E	F	G	H
2008-02-24	74	25	378	9	2.90E+12	−8.51	−0.15	2012-03-15	52	107	485	−5.8	9.2E+14	−68.04	41.85
2010-10-06	6	191	282	7	2.10E+15	−28.21	21.64	2012-03-17	318	96	505	−4.9	3.2E+14	6.34	−32.04
2010-11-15	132	26	191	37	2.30E+13	−15.86	−15.29	2012-03-21	155	161	186	4.2	1.1E+15	25.09	−49.36
2010-11-24	77	46	142	5.7	2.20E+13	−16.73	4.10	2012-03-23	326	188	700	3.8	4.3E+15	34.87	26.43
2010-11-30	76	100	333	3.3	1.30E+15	−37.16	18.51	2012-03-24	112	105	443	−7.3	3.9E+15	−16.10	−33.15
2010-12-07	265	79	203	5.6	2.20E+13	22.34	2.29	2012-03-27	319	162	1148	−13.1	4.6E+15	3.64	−42.20
2010-12-12	93	78	417	6.1	6.60E+15	−23.65	−9.66	2012-04-02	23	135	350	5.5	2.4E+15	−61.28	−44.25
2010-12-16	321	88	580	0.8	1.20E+15	42.90	53.19	2012-04-05	64	119	470	7.6	5.2E+15	−63.25	−44.76
2010-12-21	57	50	322	7	4.10E+13	−17.63	13.78	2012-04-28	131	101	469	18.2	1.4E+15	−38.42	−10.76
2011-02-25	349	63	370	12	6.50E+14	24.02	49.77	2012-04-30	7	46	316	5.6	5.3E+11	−34.43	−37.89
2011-04-09	346	55	172	0.9	2.90E+14	0.00	30.64	2012-05-19	273	27	201	6.1	5.4E+13	8.70	9.21
2011-04-15	47	31	195	−16.8	1.40E+14	−33.36	32.32	2012-05-20	144	83	273	−3.6	3.1E+14	−17.03	45.61
2011-04-17	46	75	218	5.1	5.60E+14	−32.73	25.96	2012-06-13	166	118	461	4	3.6E+15	−1.98	26.30
2011-04-17	37	33	612	19.8	7.30E+14	−16.42	18.61	2012-06-17	24	36	193	2.3	6E+13	−18.78	17.84
2011-04-19	38	44	688	−12.5	2.10E+15	−45.34	42.32	2012-06-27	61	46	618	−15.2	5.3E+14	−17.04	−0.29
2011-04-20	58	34	281	−8.7	4.80E+14	−40.88	25.43	2012-07-01	180	87	477	8.8	4.2E+14	61.90	13.30
2011-05-12	61	42	286	5.5	4.00E+14	−40.87	24.61	2012-07-03	199	87	532	−4.6	1.3E+15	46.59	34.12
2011-05-13	353	39	166	2.8	4.10E+14	−0.49	26.18	2012-08-03	310	174	304	1.2	1.9E+15	29.73	−2.48
2011-05-18	17	57	577	12.2	8.50E+14	−35.75	44.20	2012-11-09	175	276	559	4	5E+15	74.35	35.97
2011-05-29	57	29	323	−0.6	3.50E+13	−17.01	10.76	2012-11-10	189	210	762	−9.9	1.2E+15	−49.36	58.43
2011-06-11	14	73	269	2.5	1.80E+15	−6.56	42.92	2012-11-13	134	29	538	−3.1	1.1E+14	−16.35	−24.26
2011-06-14	242	36	228	11.4	4.10E+13	27.74	−13.34	2012-11-13	119	119	797	−11	1E+15	−35.48	19.22
2011-06-21	10	58	423	10.5	4.00E+13	0.00	41.60	2012-11-14	113	94	478	−10.6	7.7E+14	−56.89	−29.47
2011-06-21	0	26	203	2.1	2.30E+13	−4.09	39.21	2012-11-14	141	25	507	−26	2.4E+14	64.70	73.49
2011-07-07	85	113	361	7.2	2.30E+15	−52.81	5.59	2012-11-21	360	360	920	−16.2	2.2E+15	−21.40	42.08
2011-07-09	153	35	270	−10.5	3.00E+13	−13.21	−26.11	2013-01-23	16	51	352	3.7	3E+14	32.90	36.78
2011-07-13	142	22	174	−3.9	1.70E+14	−18.07	−20.96	2013-01-23	48	26	641	−19.8	2.4E+14	1.76	41.30
2011-07-24	310	75	317	0.1	5.70E+15	43.27	52.20	2013-02-01	92	81	126	4.2	3.5E+15	13.42	−16.00
2011-07-27	63	66	680	8	3.10E+15	−42.22	35.78	2013-04-04	288	23	460	144	1.2E+12	21.29	1.09
2011-08-10	316	28	241	−21.4	3.40E+13	26.73	21.35	2013-04-20	303	22	230	2.2	3.6E+13	−12.04	−36.03
2011-08-12	296	24	517	97.9	1.50E+14	45.06	22.23	2013-05-20	272	70	176	5.6	5.6E+14	−4.24	6.49
2011-09-05	64	84	289	0.4	2.40E+15	−82.98	8.93	2013-05-22	270	210	687	16.8	3.1E+16	−62.00	42.44
2011-09-08	325	67	351	−2	9.60E+14	46.54	48.18	2013-06-25	27	91	562	15.1	2.3E+15	−7.39	10.40
2011-10-01	10	42	175	−10.5	1.10E+15	−4.96	26.13	2013-07-16	136	0	578	6.5	1.7E+15	−3.77	3.76
2011-10-02	16	57	262	2.5	2.60E+14	−4.52	36.89	2013-08-04	52	62	305	−3.9	3.7E+14	−34.17	45.38
2011-10-31	279	74	44	0.5	8.10E+14	22.42	−1.14	2013-09-19	115	174	362	−8.4	9E+14	−68.04	41.85
2011-11-01	351	71	303	−2.6	4.30E+14	6.63	36.10	2013-10-14	340	74	298	4.3	1.5E+15	6.34	−32.04
2011-11-01	276	25	240	−6.5	1.00E+14	30.11	3.02	2013-11-05	24	126	512	1.6	3.8E+15	25.09	−49.36
2011-11-05	13	38	555	13.6	9.70E+14	−20.96	36.26	2013-11-26	49	111	671	7.7	3.1E+15	34.87	26.43
2011-11-13	102	43	208	1.1	1.10E+14	−30.33	−8.78	2013-12-01	331	159	561	−9.8	1.9E+15	−16.10	−33.15
2011-11-21	59	46	327	6.8	2.70E+14	−22.61	14.54	2013-12-02	356	39	205	2.1	1.4E+14	3.64	−42.20
2011-12-11	72	57	398	−10.5	1.10E+15	−43.23	14.00	2014-04-01	360	360	247	15.4	2.7E+15	−61.28	−44.25
2011-12-25	329	254	577	−11.5	2.30E+15	6.59	52.68	2014-04-10	270	27	399	20.3	6.3E+13	−63.25	−44.76
2012-01-23	329	221	684	35.5	5.30E+15	38.49	34.65	2014-05-12	168	144	695	−0.2	5.4E+15	−38.42	−10.76
2012-02-05	13	52	442	20.8	4.80E+14	−13.08	44.42	2014-05-29	33	47	115	1.9	4.8E+14	−34.43	−37.89
2012-02-05	359	53	588	−8	8.20E+14	−2.07	45.92	2014-06-08	50	76	362	−10.4	1E+15	8.70	9.21
2012-02-05	272	65	167	3.7	2.40E+15	19.57	0.67	2014-06-25	41	35	260	18.7	4.5E+14	−17.03	45.61
2012-02-23	292	50	468	−8.5	2.30E+14	54.45	32.44	2014-07-01	51	74	343	0.7	5.9E+14	−1.98	26.30

Column designations:

A is the event date; B is the central position angle of CME (in degrees); C is the angular size of CME (in degrees); D is the linear projection velocity of CME (in km/s); E is the CME acceleration (in m/s^2); F is the CME mass (in g); G is the φ angle (in degrees); H is the λ angle (in degrees).